Topological structures in chiral media: Effects of confined geometry

I. M. Tambovtsev ◉

Department of Physics, St. Petersburg State University, St. Petersburg 198504, Russia
and Faculty of Physics, ITMO University, 197101 St. Petersburg, Russia

A. O. Leonov

Department of Chemistry, Faculty of Science, Hiroshima University Kagamiyama,
Higashi Hiroshima, Hiroshima 739-8526, Japan
and IFW Dresden, Postfach 270016, D-01171 Dresden, Germany

I. S. Lobanov ◉

Faculty of Physics, ITMO University, 197101 St. Petersburg, Russia

Alexei D. Kiselev ◉

Laboratory of Quantum Processes and Measurements, ITMO University, 199034 St. Petersburg, Russia

V. M. Uzdin ◉

Faculty of Physics, ITMO University, 197101 St. Petersburg, Russia
and Department of Physics, St. Petersburg State University, St. Petersburg 198504, Russia

We theoretically study orientational structures in chiral magnetics and cholesteric liquid crystal (CLC) nanosystems confined in the slab geometry. Our analysis is based on the model that, in addition to the exchange and the Dzyaloshinskii-Moriya interactions, takes into account the bulk and surface anisotropies. In CLC films, these anisotropies describe the energy of interaction with external magnetic/electric field and the anchoring energy assuming that magnetic/electric anisotropy is negative and the boundary conditions are homeotropic. We have computed the phase diagram and found that the ground state of the film is represented by various delocalized structures depending on the bulk and surface anisotropy parameters, κ^b and κ^s. These include the z helix and the z cone states, the oblique, and the x helicoids. The minimum energy paths connecting the ground state and metastable helicoids and the energy barriers separating these states are evaluated. We have shown that there is a variety of localized topological structures such as the skyrmion tube, the toron, and the bobber that can be embedded in different ground states including the z cone (conical phase) and tilted fingerprint states. We have also found the structure called the leech that can be viewed as an intermediate state between the toron and the skyrmion tube.

I. INTRODUCTION

In recent years, chiral magnetic and liquid crystal (LC) systems have attracted considerable attention due to the discovery in these systems of new localized states with topological stabilization, such as skyrmions, antiskyrmions, and other local noncollinear structures [1–3]. Skyrmion states in magnetic materials have been observed in a variety of sizes ranging from nanometers to microns [4]. In these materials, small skyrmions are stabilized by the Dzyaloshinskii-Moriya interaction (DMI) caused by spin-orbit coupling. In thin two-dimensional magnetic films on the surface of heavy metals, DMI can arise due to the effect of proximity to elements with a large atomic number [5]. However, small nanosized skyrmions in few-monolayer-thick ferromagnetic (FM) films are stable only well below room temperature. For larger structures that exist at room temperature, magnetic dipole-dipole interaction turns out to be responsible for the size of the

structures and the stability against thermal fluctuations [6]. In bulk three-dimensional (3D) chiral magnetic systems with intrinsic DMI, topological magnetic structures were found in MnSi, $Fe_xCo_{1-x}Si$, FeGe, and other B20 helimagnet alloys [1]. These systems exhibit a diversity of topological structures including skyrmion tubes, baby skyrmions, magnetic bobbers, etc. [7–10].

In LCs, chiral ordering is observed in the so-called cholesteric liquid crystals (CLCs). Their properties are determined by the geometric shape and structure of the molecules. There are even CLC materials whose bulk chirality can be controlled by UV irradiation [11]. The anchoring energy characterizing the interaction of LC molecules with the bounding surfaces of CLC cells is one of the key factors determining the property of CLCs placed in thin cells. Localized topological states similar to the structures in magnetic materials are known to be formed in such chiral media [12].

In magnetic systems, new opportunities open up due to the use of artificial multilayer systems. The properties of such magnetic structures can be tuned by the layer architecture. In synthetic antiferromagnets with metallic magnetic layers separated by nonmagnetic spacers, perpendicular magnetic anisotropy, antiferromagnetic interlayer coupling, and chiral order can be controlled simultaneously. In such systems, it is possible to create small antiferromagnetic skyrmions that are stable at room temperature. This opportunity is promising for new magnetic memory technologies and other spintronic applications [13].

The feature shared by all the above systems is that the localized topological structures can be formed in chiral magnetic/LC media in confined geometry. In a planar slab structure, the boundary (anchoring) conditions together with the thickness significantly influence magnetic/orientational ordering of the ground state. As a result, stability and other characteristics of the localized topological structures in the medium will depend on these conditions. Therefore, it is important to understand the phase diagram of chiral media depending on the conditions at the bounding surfaces. The possibility of adjusting the properties by changing interactions at the boundary is also of great interest for both fundamental and technological reasons.

Another aspect that makes the problem of studying the phase diagram of chiral materials in confined geometry topical is related to the interaction between the localized topological states mediated by the polarization of the surrounding medium leading to a change in its energy. For example, the interaction between vertical and horizontal skyrmion tubes found in bulk magnetic and liquid crystal systems [14] can be explained taking into account the change in the state of the cone ordered media in which these structures are embedded [15]. Therefore, in order to understand the principles of formation of superstructures consisting of separate localized topological objects, it is also necessary to know about the ground ("vacuum") state, that is, the chiral material in which these systems are embedded.

The effects of confined geometry are most clearly manifested when the size of the system is comparable to the characteristic lengths corresponding to the order parameters of the chiral medium. In chiral magnetic and LC films and layered structures, one can expect the formation of helical states with differently oriented helix twisting axes with respect to the plane of the film. The competition between different interactions may also result in the formation of multiple metastable helical states. In particular, this is the case when the equilibrium (bulk) helix pitch is comparable to the thickness of the layers. Transitions between these states can be induced either by applying external fields or by changing other governing parameters. In addition, the field-induced transition from planar helical states to the states with out-of-plane director deformations in CLCs—the so-called Fréedericksz transition—leads to strong modification of the optical properties of CLCs used in many applications.

The stability of various states and scenarios of the transitions between them can be studied by investigating the multidimensional energy surface as a function of all variables that determine the magnetic/LC state of the [16,17] system. Local minima on the energy surface correspond to the ground

and various metastable states, saddle points determine the energy barriers between these states, and the minimum energy paths that connect different states give the most probable scenarios of the transitions between them [18]. Interactions at the boundary of the system associated with spatial confinement or the presence of interfaces in multilayers change the energy surface of the system and may affect the loci and even the number of the local minima.

In this paper, we are primarily concerned with the phase diagram and the localized topological structures in chiral magnetic/LC films with negative easy-plane anisotropy in the bulk of the film and with positive easy-axis anisotropy at the boundaries. We compute a phase diagram for ground states of chiral magnetic/LC film in surface-bulk anisotropies space, and we reveal domains of stability of various localized topological structures (skyrmion tubes, bobbers, torons [19–22]) inside the distinct phases. We consider both the continuous and the lattice models where the exchange coupling, DMI, and interaction with an external magnetic field are taken into account. The model also describes LC systems in the one-constant approximation where differences between the Frank modules are assumed to be negligible. In this case, easy-axis anisotropy at the surface will model the homeotropic anchoring conditions at the substrates of the CLC cell.

II. MODEL

We consider a film of a chiral either magnetic or nematic liquid crystal medium. The continuum model of such film is described by the energy density $\omega(\mathbf{r})$:

$$\omega(\mathbf{r}) = \mathcal{A}(\boldsymbol{\nabla} \cdot \mathbf{m})^2 - \mathcal{D}\mathbf{m} \cdot [\boldsymbol{\nabla} \times \mathbf{m}] - \mathcal{K}(\mathbf{r})(\mathbf{m} \cdot \mathbf{z})^2, \quad (1)$$

where $\mathbf{m}(\mathbf{r})$ is the vector field representing either the magnetization or the LC director, and $\mathbf{z}$ is the unit vector along the anisotropy axis z.

For magnetic systems, the first term describes the exchange interaction determined by the exchange stiffness $\mathcal{A}$, which is assumed to be homogeneous in the bulk of the film. The second term corresponds to chiral DMI with the interaction constant $\mathcal{D}$. The third contribution is the density of magnetic anisotropy described by the parameter $\mathcal{K}$ whose values inside the film and at its boundaries may differ. This difference can be caused by the proximity of another material or surface effects.

For LC systems, the value of $\mathcal{A}$ and the chiral interaction constant $\mathcal{D}$ are expressed in terms of the Oseen-Frank moduli in the one-constant approximation where all the elastic constants are assumed to be equal. In this case, the bulk value of the anisotropy constant $\mathcal{K}$ plays the role of the coupling constant for interaction with external magnetic field, whereas its value at the substrates corresponds to the anchoring energy strength.

For simulation purposes, it is a common practice to introduce discretization of the continuous model using the well-known finite-difference method. On the other hand, the magnetic moments at the nanoscale are localized on atoms at the sites of the crystallographic lattice. Then the continuous model is considered as the limiting case of a real discrete model, when the lattice constant is small compared to the
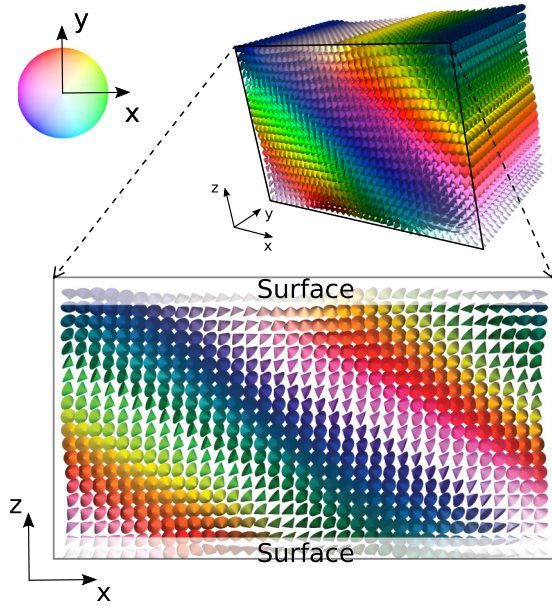
FIG. 1. Cell of a chiral medium. The top picture shows a 3D system with a rectangular grid. The bottom picture shows one layer of the 3D grid in the xz plane. The top and bottom surfaces correspond to the boundaries of the cell where additional anisotropy is added to simulate the orientationally dependent part of the surface energy (in CLCs, it is known as the anchoring energy). The color palette describes x and y projections of magnetic moments. Periodic boundary conditions (BCs) are assumed in the xy plane.

characteristic sizes of the magnetic structures. Note that different lattice models may coincide in the continuum limit.

We will consider the simplest lattice model with magnetic moments localized at the sites of a simple cubic lattice inside the rectangular cell shown in Fig. 1. This figure shows the state of an oblique spiral in a magnetic film, which will be discussed below. As discussed above, the model also describes the CLC film in the one-constant approximation. The expression for the energy of the system now reads

$$E = -\sum_{\langle i,j \rangle} [J\mathbf{m}_i \cdot \mathbf{m}_j + \mathbf{D}_{ij} \cdot (\mathbf{m}_i \times \mathbf{m}_j)] - \sum_i K_i (\mathbf{m}_i \cdot \mathbf{z})^2,$$

(2)

where $\mathbf{m}_i$ is the unit vector along either the magnetic moment or the CLC director at the site i. Summation $\langle i, j \rangle$ is performed over nearest neighbors, and the exchange parameter J is assumed to be constant.

Antisymmetric exchange (DMI) is also taken into account only between the nearest-neighbor magnetic moments. The DMI vector $\mathbf{D}_{ij}$ is directed along the line connecting the lattice sites i and j, and its length is constant, $|\mathbf{D}_{ij}| = D$. The parameter K_i defines anisotropy on the site i. The continuous parameters and the discrete ones for cubic lattice are connected as follows:

$$2a\mathcal{A} = J, \quad a^2\mathcal{D} = D, \quad a^3\mathcal{K}(\mathbf{r}) = K_i,$$

where a is the lattice constant.

In the case of vanishing anisotropy with $K_i = 0$, the ground state corresponds to the helical structure with the period [23]

$$p_0 = 2\pi / \arctan \frac{D}{J}.$$

(3)

In what follows, we consider the film of the thickness $d = p_0 = 20a$, unless otherwise specified.

In the xy plane, we shall use the periodic boundary conditions (BCs) and restrict our analysis to the case of states invariant with respect to translations along the y axis (this assumption will be relaxed in Sec. IV). The value of the period l_x along the x axis will be selected for each state to minimize its energy. Free BCs are applied for the top and bottom layers representing the cell substrates. The anisotropy K_i at the site i is different for the substrate layers and for internal sites of the sample. In the bulk of the sample, the easy-plane anisotropy $K_i = K^b \leqslant 0$ is kept fixed for all layers of the film. In LC with negative magnetic susceptibility, $\Delta\chi < 0$, the easy-plane anisotropy naturally appears as the energy of interaction of LC with the magnetic field.

Additional surface anisotropy $K^s \geqslant 0$ at the boundaries describes the surface effects that either arise from the anchoring energy of CLCs or are due to the interface with other magnetic material. Thus the total surface anisotropy is $K_i = K^b + K^s$ and the axis of the anisotropy is normal to the substrates. Positive values of K_i, $K_i > 0$, correspond to the easy axis, whereas the easy pane is described by $K_i < 0$. In what follows, the anisotropies will be expressed in terms of the dimensionless parameters: κ^b and κ^s, where $K^b = \kappa^b D^2/J$, $K^s = \kappa^s D^2/J$.

We find metastable states by minimizing the functional (2). The functional naturally appears as the energy of magnetic systems in the atomistic model, whereas the same functional gives a finite-difference discretization of the liquid crystal free energy in the continuum model (1). To find local minima of the energy, we use the direct energy minimization by the nonlinear conjugate gradient method in Cartesian coordinates $\mathbf{m}_k$ with constraints $\mathbf{m}_k^2 = 1$ [24,25].

III. DELOCALIZED PERIODICALLY MODULATED CHIRAL STRUCTURES IN THE SLAB GEOMETRY

Chiral systems may have, in addition to the ground state, several metastable states including extended structures like either helix states or chiral domain walls, and localized structures such as skyrmions, torons, hopfions, etc. [23,26]. Depending on the parameters of the system and external conditions, metastable states may change their stability or even disappear. In confined geometries, the presence of bounding surfaces and interfaces is among the factors that affect the ground and metastable states and may lead to the formation of new states that are absent in unbounded materials.

In the bulk of a chiral medium, when the uniaxial anisotropy parameter κ^b decreases, the ferromagnetic (FM) state, which is the ground state at sufficiently large positive κ^b, transforms into the helical state with the twisting axis orthogonal to the anisotropy axis at a certain threshold value of $\kappa^b > 0$. When κ^b changes its sign and $\kappa^b < 0$, the helix axis is reoriented in the direction of the axis of the easy-plane anisotropy. Similar behavior was found to occur for skyrmion tubes in an external magnetic field: a crossover of the lower energy state occurs from tubes oriented along the field to the tubes perpendicular to the field when the magnetic field decreases [26]. Note that, in all of the above helix states, the projection of the spin onto the axis of the helix is zero.
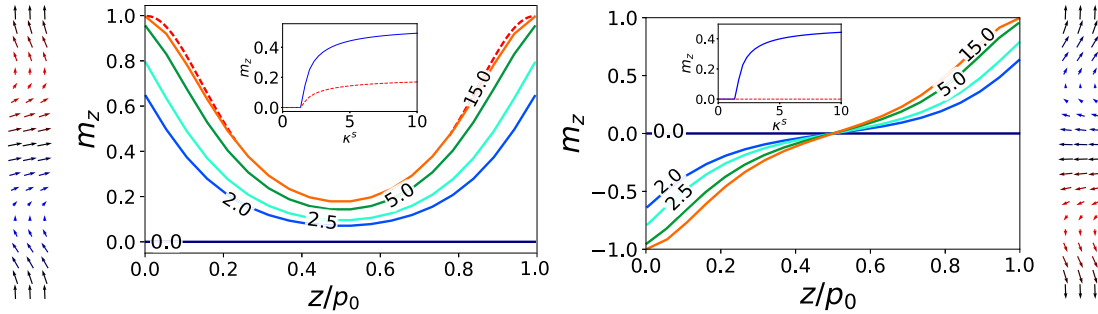
FIG. 2. z-projection of the normalized magnetization m_z for various values of surface anisotropy κ^s and volume anisotropy $\kappa^b = 0$. The left and right panels show the solutions cone-I and cone-II, respectively. The insets depict the average modulus m_z for the entire film (blue solid line) and the middle layer (red dashed line) in dependence on the κ^s. For $\kappa^s < 1.4$, the magnetization lies in the plane of the film for both cone-I and cone-II. The dashed line represents the analytical solution for semi-infinite space and $\kappa^s = \infty$.

In a film of finite thickness, the presence of bounding surfaces introduces an additional preferred direction along the normal to the surfaces that supplements the symmetry axes of the bulk material. The ground state of the confined system shown in Fig. 1 is determined by a number of factors, such as the film thickness, the anisotropy inside the film, and the surface anisotropy effects.

In a subsequent section, we shall present the phase diagram computed in the κ^b-κ^s parameter space. In particular, our analysis shows that there is a new ground state formed in certain regions of the parameters. In what follows, this state will be referred to as the *oblique helicoid (cone) state*. Such a cone state can be viewed as an intermediate state between the spiral states with the twisting axes either parallel or normal to the film substrate (the *x-helicoid* and the *z-helix*, respectively). The formation of an inclined cone state is a direct consequence of confined geometry. Note that, in bulk materials, the competition between local cubic and exchange anisotropies may also lead to inclined spiral states [27].

A. z-helix and z-cone states

Let us consider the film shown in Fig. 1 with the easy-plane anisotropy in the bulk of the film with $\kappa^b \leqslant 0$. At negligibly small κ^b, the ground state is the z-helix with the period p_0 (3). In a semi-infinite space, $z \geqslant 0$, with the strong easy-axis anisotropy at the boundary, where all the moments are kept normal to the bounding plane, $z = 0$, the ground state for a chiral medium can be found analytically. To this end, it is enough to find the minimizer for the functional (1) that meets the corresponding boundary conditions at $z = 0$. The ground-state configuration is uniform in the xy plane and can be described by the polar and the azimuthal angles $\theta(z)$ and $\phi(z)$, where $\theta(z)$ is the angle between the magnetic moment (director) and the z-axis. The boundary conditions for θ are as follows:

$$\theta(z)|_{z=0} = 0, \quad \theta(z)|_{z=\infty} = \frac{\pi}{2}$$

and the solution reads

$$\theta(z) = 2\arctan\exp\left|\frac{\mathcal{D}}{2\mathcal{A}}z\right| - \frac{\pi}{2}, \quad \phi(z) = \phi_0 + \frac{\mathcal{D}}{2\mathcal{A}}z,$$

where ϕ_0 is the value of the angle ϕ at $z = 0$. This solution represents the magnetic moments (director field vector) that uniformly rotate about the z axis whereas their z-projection decreases with z.

In the film of finite thickness with arbitrary anisotropy κ^s, the solution can be obtained numerically. Figure 2 shows the z dependence of the z-projection of the magnetic moment on z (the distance from the lower boundary along its normal) and the corresponding magnetic configurations.

The left (right) panel depicts the symmetric (antisymmetric) conical solution that will be referred to as cone-I (cone-II). For cone-II, the z-projection of the moment vanishes in the middle of the film and, in thin films, is characterized by pronounced variations in m_z so that its energy is typically larger as compared to cone-I. However, similar to the stability of one-dimensional domain walls, this configuration can be stable due to topological reasons.

In thick films, where the z-projection of the moment is close to zero in the middle layer for both the symmetric and antisymmetric solutions, the energies of cone-I and cone-II are the same. Note that the sign of the z-projection of the director has no physical meaning for LC systems, and the director configurations on both surfaces are the same for cone-II in the strong anchoring limit $\kappa^s \to \infty$. However, the solutions exist and represent topologically different orientational structures in LC systems as well.

At nonvanishing plane anisotropy with $\kappa^b < 0$, the transition from the z-helix state (the state without z projection) to the z-cone state takes place at a certain surface anisotropy κ^s which is an increasing function of $|\kappa^b|$. The z-helix and z-cone structures bear close resemblance to those involved in the Fréedericksz transition that occurs in LC under the action of electric or magnetic fields. Note that both the z-helix and the z-cone exist at least as metastable states in the entire range of the parameters κ^b and κ^s. As will be shown later on, the transition from the z-helix to the cone-I state, which occurs as κ^s increases, involves the transition to a new ground state, which might be called the oblique helicoid state.

B. x-helicoid

In an unbounded sample with small anisotropy $\kappa^b > 0$ along the z-axis, the ground state is the x-helix with the pitch
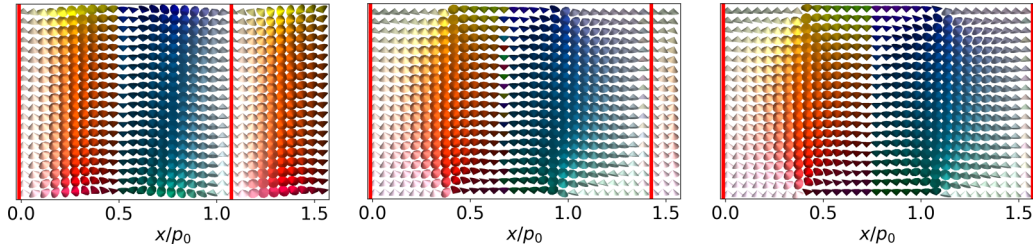
FIG. 3. x-helicoid state for vanishing bulk anisotropy $\kappa^b = 0$ and different values of the surface anisotropy κ^s: 0 (left), 10 (middle), and 20 (right). One pitch of x-helicoid in the magnetic film is shown between the red lines. For LC, the pitch is twice as small.

p slightly larger than p_0. At $\kappa^b < 0$, this is no longer the case. However, in thin films it turns out that the boundary conditions with $\kappa^s > 0$ have a stabilizing effect on the x-helicoidal structure provided the magnitude of the negative anisotropy κ^b is sufficiently small.

For the system shown in Fig. 1, calculations were carried out using the periodic boundary conditions along the x and y axes. We shall assume that the states are invariant with respect to the translations along the y axis (nonhomogeneous states corresponding to fingerprint patterns that will be considered in the section dealing with localized topological structures).

Given the value of l_x, the calculations were performed to compute the local minimum of energy (2). This energy minimum depends on the period l_x, and the corresponding structure is characterized by the pitch $p_x = l_x/n$, where n is the spiral pitch number per period l_x. Minimizing the energy with respect to the pitch p_x gives the metastable state corresponding to the specified anisotropies κ^b and κ^s.

The helix pitch p_x depends on the surface anisotropy and is an increasing function of κ^s. This can be seen from Fig. 3, which shows the orientational structures in the x-z plane computed for three values of $\kappa^s \in \{0, 10, 20\}$ in the absence of bulk anisotropy $\kappa^b = 0$. Referring to Fig. 3, the pitch is increased by more than one and a half times.

Figure 4 presents the dependence of the pitch ratio $\lambda \equiv p/p_0$ on the surface anisotropy κ^s computed at different values of the ratio (the so-called confinement ratio) of the film thickness d and the equilibrium pitch p_0, d/p_0, and $\kappa^b = 0$. It can be seen that, for small anisotropy κ^s, the pitch is close to p_0 for all thicknesses. In thick films with a sufficiently large confinement ratio, the helix pitch grows with the surface anisotropy
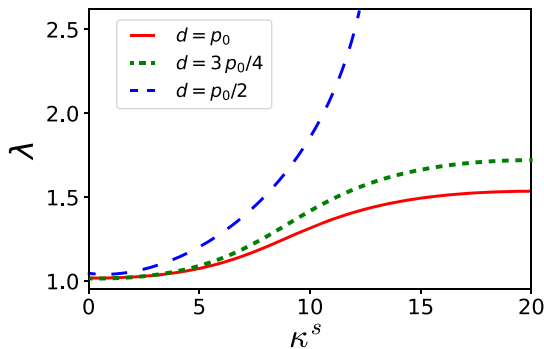
approaching the constant value in the limit of strong anchoring where $\kappa^s \to \infty$. By contrast, in thin films with $d < p_0$, the helix pitch diverges with surface anisotropy, which leads to an unwinding of the x-helicoid. Our findings agree quantitatively with the results of [28] on equilibrium configurations and the phase diagram of thin LC films with homeotropic boundary conditions.

Note that a similar LC structure was studied in [29], where the analytical solution was derived in the case of strong surface anisotropy. An important assumption taken in this work is that the LC director is normal to the x axis. This assumption, however, cannot be used to describe the x-helicoid structure. In our calculations, for thick films with $\kappa^b = 0$, the total magnetization along the x axis initially decreases with κ^s due to the ordering of the surface layer moments along the normal to the boundary. Surprisingly, after reaching the minimum at $\kappa^s \simeq 5$, the x-projection starts growing due to the tilt of the moments in the layers closest to the surface layer. Such tilted structures modulated along the in-plane direction have been reported in [30].

C. Oblique helicoid state

Now we consider the z-helix and z-cone states in the range of anisotropy parameters where $\kappa^b < 0$ and $\kappa^s > 0$. The transition between these states occurs as the anisotropy κ^s increases. Note that the Fréedericksz transition in cholesteric LCs driven by external magnetic or electric fields involves similar states. Such a transition between in-plane and out-of-plane director structures in LC can be either continuous or jumplike depending on the parameters of the system [31].

In contrast to the Fréedericksz transition, in our model we found that the transition from the z-helix state to the z-cone state involves the new additional state—the so-called oblique helicoid state shown in Figs. 1 and 5. Moreover, this state appears to be a ground state in a certain range of the anisotropies κ^s.

This oblique helicoid state is characterized by the spatial period p of the structure and the inclination angle α from the z-axis. Both the inclination of the helicoid and its period along the x axis depend on the anisotropy parameters $\kappa^b < 0$ and $\kappa^s > 0$.

Figure 5 shows the oblique spiral states in the absence of bulk anisotropy, $\kappa^b = 0$, computed at two different values of the surface anisotropy $\kappa^s = 10$ and 20. It can be seen that, at $\kappa^b = 0$, the larger the surface anisotropy is, the smaller is the inclination angle.

FIG. 4. The ratio of the pitch p_x of the x-helicoid in the film and in the bulk medium $\lambda = p_x/p_0$ as a function of the surface anisotropy κ^s for films of different thickness d. Volume anisotropy $\kappa^b = 0$.
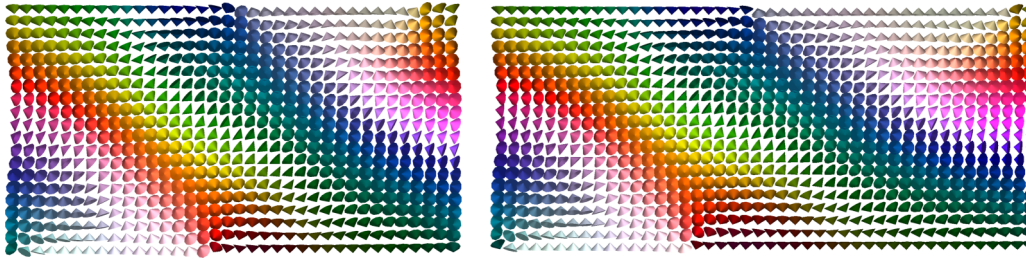
FIG. 5. Oblique helicoid states at $\kappa^b = 0$ with $\kappa^s = 10$ (left panel) and $\kappa^s = 20$ (right panel).

Now we discuss how the inclination angle can be computed. Given the twisting axis $\mathbf{q}$, the spatial dependence of the magnetic moment (LC director) in the bulk will be determined by the projection $s = \mathbf{r} \cdot \mathbf{q}/q^2$ of vector $\mathbf{r}$ on the axis $\mathbf{q}$:

$$\mathbf{m}(\mathbf{r}) = \mathbf{m}(\mathbf{r}_0 + s\mathbf{q}) = \mathbf{m}(s)$$

for all s and any fixed $\mathbf{r}_0$. Therefore, the elements of the gradient matrix of the magnetization can be written in the following form:

$$(\nabla \mathbf{m})_{ij} \equiv \nabla_i m_j = \frac{q_i}{\mathbf{q}^2} \frac{dm_j}{ds}.$$

In the discrete model with the energy (2), the gradient matrix is represented by finite differences and has small deviations from this form. To reduce the errors, $\mathbf{q}$ is approximated by the left-singular vector of the gradient matrix corresponding to the largest singular value. After computing the helix axis $\mathbf{q}$, we obtain the inclination angle α in the form

$$\alpha = \arccos \frac{\mathbf{q} \cdot \mathbf{z}}{\mathbf{q}^2}. \tag{4}$$

The oblique helicoid is formed as a result of the confined geometry of the system and exists, as the ground state, only at certain values of the film thickness d. The inclination angle α and the lateral period p_x will also depend on the film thickness. Figure 6 shows the dependence of the angle α and the dimensionless spatial period $\lambda = p_x/p_0$ on the film thickness. It can be seen that the period is a monotonically increasing function of the thickness d, whereas the inclination angle
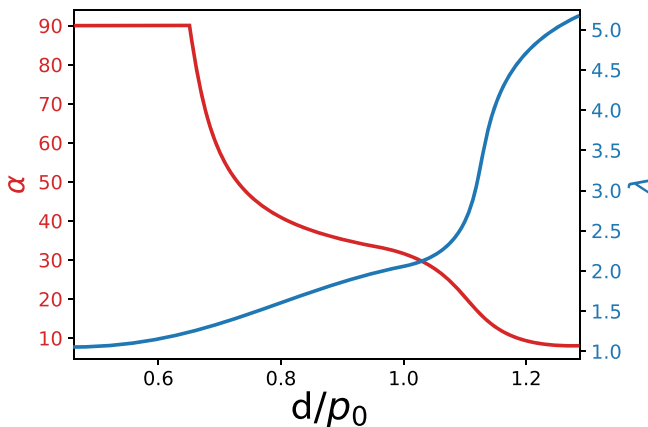
lowers with the thickness so that the oblique cone transforms into the z-cone in the thick film limit. As the thickness decreases, the oblique spiral approaches the x-helicoid formed at the critical value of the thickness $d \approx 0.65 \, p_0$.

Just as in the x-helicoid, metastable configurations of the oblique helicoid are evaluated in the boxes of different sizes to obtain an optimal value of p_x corresponding to the minimum energy. The x-helicoid and the oblique helicoid states coexist as metastable states and differ in both the period and the energy. To assess the stability of these states, it is useful to construct the energy surface of the system and find the minimum energy path (MEP) between the states. The maximum along the MEP gives the energy barrier for the transition between states. The MEP can be found using the geodesic nudged elastic band method [32] or other special methods [33,34]. This approach was used to study the stability of magnetic systems [35–37] as well as LC structures [16–18].

Figure 7 shows the MEPs between the state of the x-helicoid and the oblique helicoid computed at fixed box size with the dimensionless period $\lambda = 1.1$ and the surface anisotropy $\kappa^s = 5$. Solid and dashed lines represent the results evaluated at different values of the bulk anisotropies: $\kappa^b = -0.05$ and -0.1, respectively. It is illustrated that the x-helicoid being a ground state at sufficiently small $|\kappa^b|$ becomes metastable when the magnitude of κ^b increases.

By contrast to the solid and dashed lines, the results represented by the dash-dotted line in Fig. 7 are obtained by

FIG. 6. Inclination angle α and dimensionless period $\lambda = p_x/p_0$ (p_0 is the equilibrium value of pitch) of the oblique cone as a function of the film thickness d computed at $\kappa^b = -0.2$ and $\kappa^s = 0$.
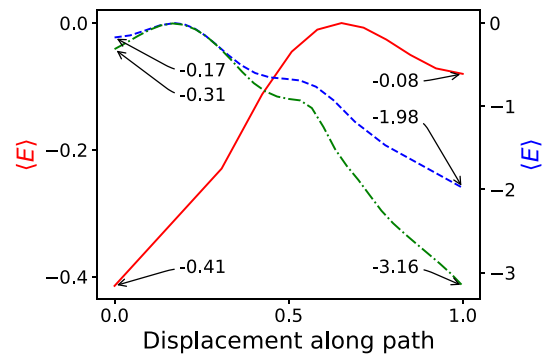

FIG. 7. The MEPs between the oblique spiral and the x-helicoid at $\kappa^b = -0.05$ (left axis, solid line) and $\kappa^b = -0.1$ (right axis, dashed line) for the fixed surface anisotropy $\kappa^s = 5$ and the fixed pitch $\lambda = 1.1$. The dash-dotted line is a MEP with optimization of the pitch along the path as shown in Fig. 8. The mean spin energy $\langle E \rangle$ is presented in units of $J \times 10^{-5}$ and is counted from the barrier energy.
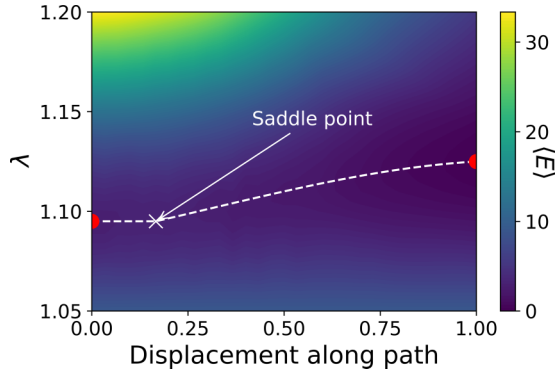
FIG. 8. Energy as a function of the pitch λ and the reaction coordinate for the transition from the x-helicoid (left border) to the oblique spiral (right side) at $\kappa^b = -0.1$, $\kappa^s = 5$. The MEP is marked by the dashed line, and the cross marker indicates the transition state. The mean spin energy $\langle E \rangle$ is measured in units of $J \times 10^{-5}$ and is counted from the lowest energy.

minimizing the energy over the in-plane period p_x. Figure 8 shows a heat map visualizing the energy along the MEP between the states of the x-helicoid and the oblique helicoid. Each line at fixed λ on the map represents a MEP computed for the fixed box size enforcing the pitch. The local coordinates (displacement) for the x-helicoid and the oblique helicoid on the MEP are zero and unity, respectively. The pitch corresponding to the minimum energy of the x-helicoid and the oblique helicoid is $\lambda = 1.10$ and 1.12, respectively. Referring to Fig. 8, it is reasonable to assume that the dependence of MEPs on the pitch is continuous. So, we can use the two-dimensional surface shown in Fig. 8 to construct the MEP that takes into account the pitch as an additional degree of freedom and computed by performing minimization over the pitch λ. This optimal MEP represents a transition involving the chiral structures with varying pitch during the transformation from the x-helicoid to the oblique helix. Both the initial and the final structures for this transition have the lowest possible energy at the given system parameters. The corresponding energy along such a path is shown in Fig. 8 with the dashed line (see also the dash-dotted line in Fig. 7).

The values of the energy barriers obtained from the MEP connecting the states can be used to assess their stability. Real transitions between the states can occur through a local transformation of the structure near defects, and the propagation of the new phase into the bulk, similar to the motion of domain walls, will take place without energy consumption.

The states associated with an inclined helix in chiral media have been observed experimentally in liquid crystal systems [28,38]. They belong to the class of the cholesteric finger structures.

The behavior of such systems under changing external conditions and transitions between such states can be described using our model. To this end, note that, in LC systems, the effective bulk anisotropy parameter κ^b is controlled by the external fields such as the electric field. In LCs experimentally studied in [39], the LC configuration transition from an oblique spiral to a z-cone was observed when the magnitude of the "easy-plane" anisotropy with $\kappa^b < 0$ gradually increases. Figure 9 shows the evolution of the LC states when κ^b changes
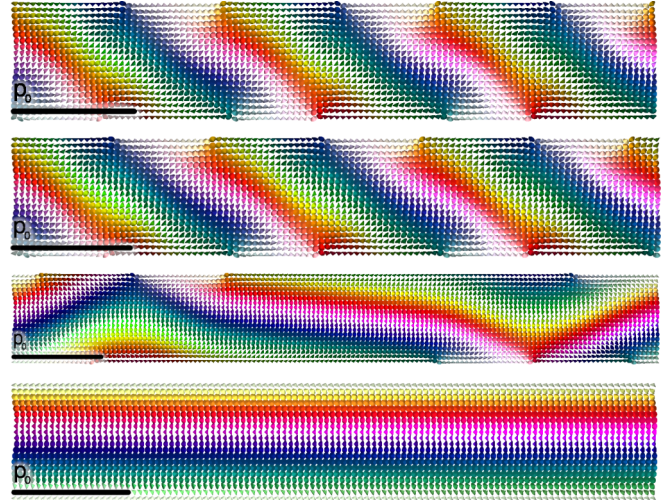

FIG. 9. The alteration of the oblique spiral when the bulk anisotropy κ^b runs through values 0 (top), -0.2, -0.8, and -2.4 (bottom) assuming constant surface anisotropy $\kappa^s = 11$.

accordingly. It can be seen that an increase in the angle of inclination followed by the transformation into the z-helix found in our simulation is in excellent agreement with the electric field dependence of the director distribution experimentally observed in a cholesteric LC [39].

D. Phase diagram

The phase diagram presented in Fig. 10 shows the ground states of the confined chiral system in the κ^b-κ^s plane. In the region where $\kappa_b \leqslant 0$ and $\kappa_s \geqslant 0$ depicted in Fig. 10, the z-helix and cone-I are generally both metastable (locally stable). The regions where the z-helix and cone-I correspond to the ground-state structure are shown in Fig. 10 in light blue
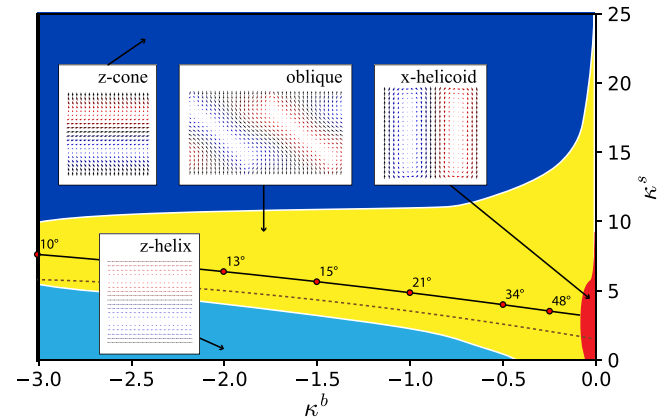

FIG. 10. Phase diagram of a confined chiral medium in the κ^b-κ^s plane (the bulk anisotropy–surface anisotropy plane) computed at the film thickness $d = p_0$. The magnetic/LC configurations are illustrated in the insets. The curve of equal energies for the z-helix and the z-cone is indicated as the dashed line. The black solid line marks the states with the maximum inclination angle α of the axis of the oblique helicoid.
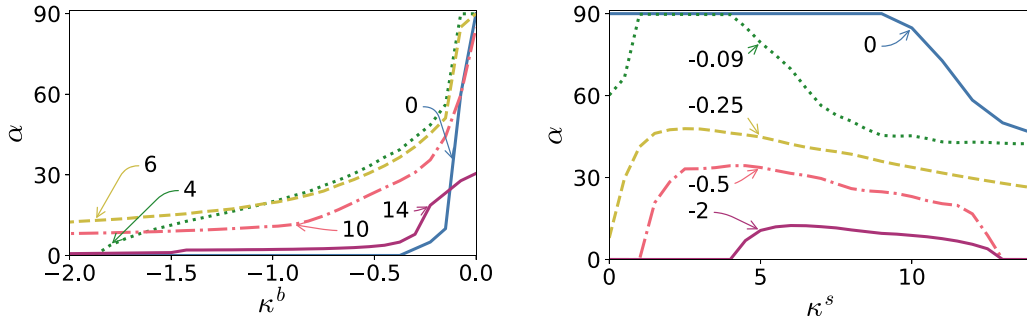
FIG. 11. Inclination angle α (in degrees) for the oblique cone as a function of the bulk anisotropy κ^b (left) and the surface anisotropy κ^s (right). The limiting cases with $\alpha = 0°$ and $90°$ correspond to the z-cone and to the x-helicoid, respectively.

and blue, respectively. The insets illustrate the magnetic (LC) configurations for each state.

The black dotted line indicates the curve in the κ^b-κ^s plane where the energies of these structures are equal. It can be seen that, given the value of κ_b, the transition from the z-helix to cone-I will take place when the surface anisotropy parameter κ_s exceeds its threshold value. This value is an increasing function of the magnitude $|\kappa^b|$.

An important point is that, as is shown in the phase diagram, the above transition involves the oblique helicoid as an intermediate state that appears to be the ground state in the yellow region. As a result, referring to Fig. 10, the z-helix state transforms into the oblique helicoid when κ_s increases at fixed bulk anisotropy parameter κ_b. In this case, the inclination angle α defined by Eq. (4) first increases from zero up to its maximum value indicated on the black solid line in Fig. 10. After that, the angle decreases down to zero at the boundary of the region where the ground state turns into cone-I. Since the oblique helicoid exists only in the yellow region, at sufficiently large values of κ_b (this high field region is not shown in Fig. 10), the transition from z-helix to cone-I will occur bypassing the oblique spiral.

In the low bulk anisotropy region, which is colored in red and where the anisotropies κ^b and κ^s are both sufficiently small, it turned out that the ground state is the x-helicoid. As was previously discussed, this structure can be stabilized by the boundary conditions provided the magnitude of κ^b is sufficiently small. From Fig. 10, an increase in the surface anisotropy κ^s leads to the transition from the x-helicoid to the oblique spiral state.

In Fig. 11 we show how the inclination angle, α, of the oblique helicoid given by Eq. (4) depends on the anisotropy parameters. The graphs on the left present dependencies of α on the bulk anisotropy parameter computed at different values of the surface anisotropy κ^s. It can be seen that the angle α is a decreasing function of the magnitude of the bulk anisotropy parameter $|\kappa_b|$. Its maximal value is close to $\pi/2$ provided the value of κ^s is below 10. The angle α vanishes in the high field limit where $|\kappa^b|$ is sufficiently large.

The curves representing the dependencies of the angle α on the parameter κ^s at various values of the bulk anisotropy κ^b are shown on the right. When $|\kappa^b|$ is small, the maximum value of the angle is $90°$ corresponding to the state of the x-helicoid. An increase in $|\kappa^b|$ results in a reduction of the maximum value in accordance with the phase diagram in Fig. 10.

IV. LOCALIZED TOPOLOGICAL STRUCTURES

There are a variety of metastable localized structures that can be formed in different regions of the phase diagram shown in Fig. 10. We begin with the domains where the ground states are invariant with respect to in-plane translations. Such states include the z-helix and the z-cone. In contrast to the above analysis restricted to the structures that are uniform along the y-axis, now we consider the states that are nonuniform in the y-direction giving rise to localized topological structures embedded in the uniform background.

Figure 12 presents three types of localized magnetic configurations, referred to as the skyrmion tube, the leech, and the toron. The orientation of the magnetic moments displayed in Fig. 12 differs from the ground state by an angle larger than $15°$. Similar structures called "baby skyrmions" have been experimentally observed in homeotropically oriented LC cells [19].

The magnetic configuration called the skyrmion tube is shown in Fig. 12(a). This structure resembles vertical skyrmion tubes in bulk chiral magnets in a magnetic field [15,26]. In moderate magnetic field, the magnetically induced conical phase is found to impose a twisting effect on the tube leading to the crankshaft structure.

Another structure shown in Fig. 12(c) is called the toron following notation introduced in [20]. It is located in the bulk of the film touching the boundary surfaces. Just as in the torons in magnetic systems [21], in such structures magnetic
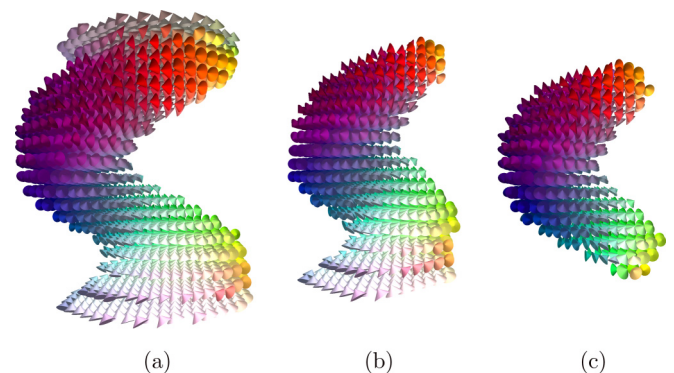

FIG. 12. Topological structures found in the conical phase: skyrmion tube (a), leech (b), and toron (c). Spins oriented in the same way as in the cone are not shown.
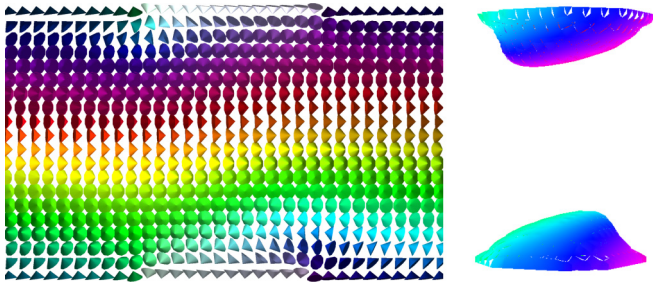
FIG. 13. Bobber in the conical phase, yz projection. Left: all spins of one layer are shown. Right: level surface of constant $m_z = 0.85$.

moments on the surfaces are kept intact, whereas in the horizontal section at the middle of the film, the structure bears a close resemblance to the skyrmion tube. Although the toron in Fig. 12(c) resembles the one described in [20], in our case the torons are surrounded by the conical phase that, similar to the skyrmion tube, induces twists of the torons.

The structure depicted in Fig. 12(b) presents the intermediate case between the skyrmion tube and the toron: it is attached only to one of the boundaries and, just as with the toron, has a tail [Fig. 12(c)]. This structure is called a leech. Note that the leechlike structures formed in asymmetric LC cells were previously described in [12,20] as skyrmion/toron hybrids. In contrast to the hybrids, our structures are formed in symmetric cells and are twisted due to the presence of the surrounding conical phase.

In addition, we have found the structures localized near one of the bounding surfaces. In analogy with magnetic chiral bobbers in thick magnetic films [21,22], we call them bobbers. The structure of the bobber is shown in Fig. 13. The level surface for m_z is depicted in the right part of Fig. 13. The colors of this surface, similar to Fig. 1, indicate the orientation of the spins in the x-y plane, which is specified by the azimuthal angle.

Figure 14 shows the regions of local stability for different localized topological states in the phase diagram. It can
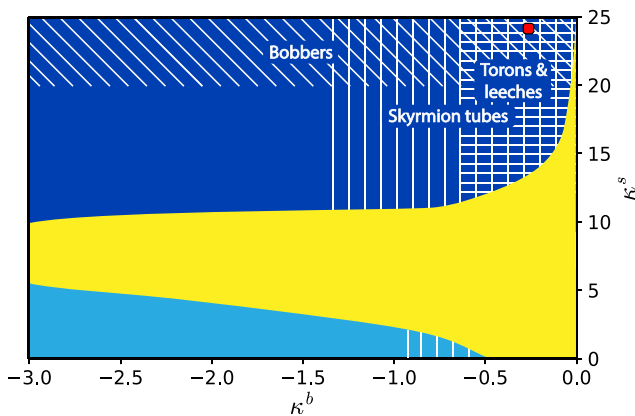

FIG. 14. Domains in which various types of metastable topological states exist: skyrmion tubes, vertically shaded area; torons and leeches, horizontally shaded area; bobbers, obliquely shaded area.
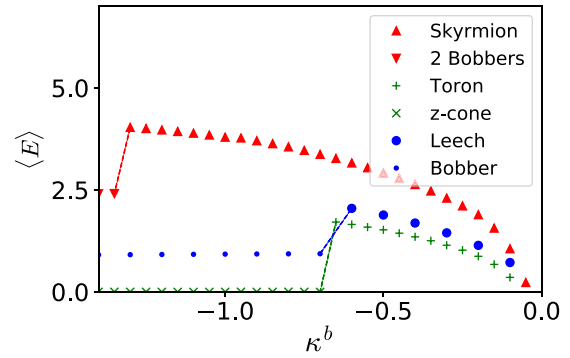

FIG. 15. Energy from z-cone on κ^b for the skyrmion, toron, and leech at $\kappa^s = 24$. With the increase of the absolute value of the anisotropy, the energy of the localized states grows until the destruction of the state. The new state with the lower energy forms, and the moment of the break is shown by an arrow with the new state deception.

be seen that there is a domain located in the conical phase where all of the above states coexist simultaneously. The point marked by the red filled square in Fig. 14 corresponds to the configurations shown above in Figs. 12 and 13.

Referring to Fig. 15, the toron is the state of the lowest energy. Its energy increases with the magnitude of the bulk anisotropy κ^b, whereas its transverse size decreases leading to elongation of the shape along the z-axis. At $\kappa^b \approx -0.6$, the toron becomes unstable and transforms into the conical phase. Despite the fact that the energy of the skyrmion tube is larger than that of the toron, it remains locally stable up to higher values of $|\kappa^b|$. When $|\kappa^b|$ increases, its central part becomes thinner. The tube loses its stability at $\kappa^b \approx -1.45$ and decays into a pair of bobbers located near the upper and lower bounding surfaces. (Videos illustrating the above behavior of the toron and the skyrmion tube depending on the bulk anisotropy κ^b computed at $\kappa^s = 24$ can be found in the Supplemental Material [40]).

The leeches and torons share the same threshold value of $|\kappa^b|$ above which they become unstable. Above the threshold, the leeches will transform into single bobbers whereas the torons will disappear.

Note that, as is shown in Fig. 15, the doubled energy of the single bobber is noticeably less than the energy of the bobber pair formed during the decay of the skyrmion tube. It can be shown that the energy of the bobber pair as a function of the distance separating the bobbers exhibits two local minima. One of the minima at the cell thickness d corresponds to the metastable state, whereas the energy minimum at a larger
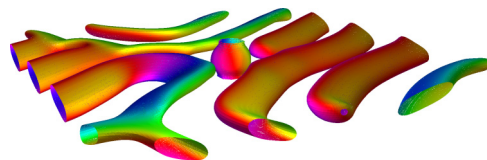

FIG. 16. Skyrmion in the tilted fingerprint state. The surface marks spin with constant $m_z = 0$. $\kappa^b = 0$, $\kappa^s = 18$. The spin orientation is represented by color.
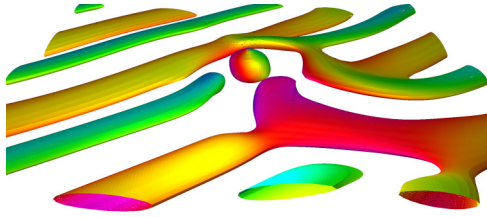
FIG. 17. Toron in the tilted fingerprint state. The surface marks spin with constant $m_z = -0.1$. $\kappa^b = -0.05$, $\kappa^s = 24$. The spin orientation is represented by color.

distance (it can be estimated at about $3.6d$) appears to be less than the doubled energy of the single bobber (the energy in the large distance limit).

In the region of the phase diagram where the ground state is the oblique spiral (indicated by yellow in Fig. 14), the localized topological structures can be embedded into the fingerprints structure. Examples of such configurations for the cases of the skyrmion tube and the toron are shown in Figs. 16 and 17, respectively. The figures present the surface level for m_z ($m_z \approx 0.97$) colored depending on the azimuthal angle. When the skyrmion tube and the toron are surrounded by the ferromagnetic phase, their structure is completely analogous to the corresponding configurations in the homeotropic LC cell.

The video in the Supplemental Material [40] shows how the skyrmion tube and toron states change when the bulk anisotropy κ^b varies at the fixed surface anisotropy $\kappa^s = 24$. The skyrmion tube shrinks as the magnitude of κ^b increases and ultimately transforms into a couple of bobbers. The toron is shrinking with $|\kappa^b|$ and eventually disappears.

V. CONCLUSION

In this work, we have analyzed the model describing both a magnetic nanosystem and the chiral liquid crystals in the one constant approximation to study how the effects of confined geometry affect the orientational structures and their stability. In this model, the surface part of the energy is represented by the surface anisotropy term proportional to κ^s that, in liquid crystal systems, corresponds to the anchoring energy (we have considered the case of homeotropic boundary conditions). The

bulk anisotropy term is proportional to κ^b and describes the energy of interaction with the external magnetic field (for liquid crystals, this term implies negative anisotropy of the magnetic susceptibility, $\Delta\chi < 0$).

We have computed the phase diagram (see Fig. 10) and have found that the ground state can be represented by different types of delocalized structures such as the z-helix, the z-cone, the x-helicoid, and the oblique helicoid depending on the values of the surface and bulk anisotropy parameters.

Though the z-helix and z-cone states both exist in any combinations of the parameters, they represent the ground state in different regions of the κ^s-κ^b plane shown in Fig. 10. The oblique helicoid is found to be an intermediate state for the transition from the z-helix to the z-cone induced by an increase in the surface anisotropy at sufficiently large $|\kappa^b|$.

It is shown that the inclination angle of the oblique spiral decreases with the magnitude of the bulk anisotropy reaching either the z-helix or the z-cone states when the angle vanishes. The inclination angle increases as $|\kappa^b|$ approaches zero and, in the low field region where $|\kappa^b|$ is small, the oblique helicoid transforms into the x-helicoid. In this region, the oblique spiral and the x-helicoid may coexist having different lateral periods p_x. We have studied the MEP connecting these states and evaluated the barrier energy separating them. Our results for the transition between the oblique spiral and the z-cone are found to be in excellent agreement with the director distribution experimentally observed in a cholesteric LC [39].

We have shown that the known localized topological structures, such as the toron, the skyrmion tube, and the bobber, can be formed in the z-cone ground state (the conical phase). In addition, there is a new state called the leech that is the intermediate state between the toron and the skyrmion tube. When the magnitude of the bulk anisotropy increases, the skyrmion tube, the leech, and the toron are transformed into a couple of bobbers, a single bobber, and the z-cone, respectively. We have also found that, in the stability region of the oblique spiral, the skyrmion and the toron can be embedded in the fingerprint structure by forming the homeotropically oriented zone around them.

[1] N. Nagaosa and Y. Tokura, Topological properties and dynamics of magnetic skyrmions, Nat. Nanotechnol. **8**, 899 (2013).

[2] A. Nych, J. I. Fukuda, U. Ognysta, S. Žummer, and I. Muševič, Spontaneous formation and dynamics of half-skyrmions in a chiral liquid-crystal film, Nat. Phys. **13**, 1215 (2017).

[3] P. J. Ackerman and I. I. Smalyukh, Diversity of Knot Solitons in Liquid Crystals Manifested by Linking of Preimages in Torons and Hopfions, Phys. Rev. X **7**, 011006 (2017).

[4] R. Wiesendanger, Nanoscale magnetic skyrmions in metallic films and multilayers: A new twist for spintronics, Nat. Rev. Mater. **1**, 16044 (2016).

[5] A. Fert, N. Reyren, and V. Cros, Magnetic skyrmions: advances in physics and potential applications, Nat. Rev. Mater. **2**, 17031 (2017).

[6] F. Büttner, I. Lemesh, and G. S. D. Beach, Theory of isolated magnetic skyrmions: From fundamentals to room temperature applications, Sci. Rep. **8**, 4464 (2018).

[7] P. J. Ackerman, T. Boyle, and I. I. Smalyukh, Squirming motion of baby skyrmions in nematic fluids, Nat. Commun. **8**, 673 (2017).

[8] F. Zheng, F. N. Rybakov, A. B. Borisov, D. Song, S. Wang, Z. A. Li, H. Du, N. S. Kiselev, J. Caron, A. Kovács, M. Tian, Y. Zhang, S. Blügel, and R. E. Dunin-Borkowski, Experimental observation of chiral magnetic bobbers in b20-type fege, Nat. Nanotechnol. **13**, 451 (2018).

[9] S. Schneider, D. Wolf, M. J. Stolt, S. Jin, D. Pohl, B. Rellinghaus, M. Schmidt, B. Büchner, S. T. B. Goennenwein, K. Nielsch, and A. Lubk, Induction Mapping of the 3d-Modulated Spin Texture of Skyrmions in Thin Helimagnets, Phys. Rev. Lett. **120**, 217201 (2018).

[10] D. Foster, C. Kind, P. J. Ackerman, J.-S. B. Tai, M. R. Dennis, and I. I. Smalyukh, Two-dimensional skyrmion bags in liquid crystals and ferromagnets, Nat. Phys. **15**, 655 (2019).

[11] T. N. Orlova, R. I. Iegorov, and A. D. Kiselev, Light-induced pitch transitions in photosensitive cholesteric liquid crystals: Effects of anchoring energy, Phys. Rev. E **89**, 012503 (2014).

[12] I. I. Smalyukh, Review: Knots and other new topological effects in liquid crystals and colloids, Rep. Prog. Phys. **83**, 106601 (2020).

[13] W. Legrand, D. Maccariello, F. Ajejas, S. Collin, A. Vecchiola, K. Bouzehouane, N. Reyren, V. Cros, and A. Fert, Room-temperature stabilization of antiferromagnetic skyrmions in synthetic antiferromagnets, Nat. Mater. **19**, 34 (2020).

[14] H. R. O. Sohn, S. M. Vlasov, V. M. Uzdin, A. O. Leonov, and I. I. Smalyukh, Real-space observation of skyrmion clusters with mutually orthogonal skyrmion tubes, Phys. Rev. B **100**, 104401 (2019).

[15] S. M. Vlasov, A. O. Leonov, and V. M. Uzdin, Skyrmion flop transition and congregation of mutually orthogonal skyrmions in cubic helimagnets, J. Phys.: Condens. Matter **32**, 185801 (2020).

[16] S. S. Tenishchev, A. D. Kiselev, A. V. Ivanov, and V. M. Uzdin, Multiple minimum-energy paths and scenarios of unwinding transitions in chiral nematic liquid crystals, Phys. Rev. E **100**, 062704 (2019).

[17] A. V. Ivanov, P. F. Bessarab, E. V. Aksenova, V. P. Romanov, and V. M. Uzdin, Energy surface and minimum energy paths for freedericksz transitions in bistable cholesteric liquid crystals, Phys. Rev. E **93**, 042708 (2016).

[18] S. S. Tenishchev, I. M. Tambovtcev, A. D. Kiselev, and V. M. Uzdin, Hysteresis and freedericksz thresholds for twisted states in chiral nematic liquid crystals: Minimum-energy path approach, J. Mol. Liq. **325**, 115242 (2021).

[19] P. J. Ackerman, R. P. Trivedi, B. Senyuk, J. van de Lagemaat, and I. I. Smalyukh, Two-dimensional skyrmions and other solitonic structures in confinement-frustrated chiral nematics, Phys. Rev. E **90**, 012505 (2014).

[20] J.-S. B. Tai and I. I. Smalyukh, Surface anchoring as a control parameter for stabilizing torons, skyrmions, twisted walls, fingers, and their hybrids in chiral nematics, Phys. Rev. E **101**, 042702 (2020).

[21] A. O. Leonov and K. Inoue, Homogeneous and heterogeneous nucleation of skyrmions in thin layers of cubic helimagnets, Phys. Rev. B **98**, 054404 (2018).

[22] F. N. Rybakov, A. B. Borisov, S. Blügel, and N. S. Kiselev, New Type of Stable Particlelike States in Chiral Magnets, Phys. Rev. Lett. **115**, 117201 (2015).

[23] S. D. Yi, S. Onoda, N. Nagaosa, and J. H. Han, Skyrmions and anomalous Hall effect in a Dzyaloshinskii-Moriya spiral magnet, Phys. Rev. B **80**, 054416 (2009).

[24] I. Lobanov and V. Uzdin, The lifetime of micron scale topological chiral magnetic states with atomic resolution, Comput. Phys. Commun. **269**, 108136 (2021).

[25] I. Lobanov, M. Potkina, and V. Uzdin, Stability and lifetimes of magnetic states of nano- and microstructures (Brief Review), JETP Lett. **113**, 801 (2021).

[26] A. O. Leonov, A. N. Bogdanov, and K. Inoue, Toggle-switch-like crossover between two types of isolated skyrmions within the conical phase of cubic helimagnets, Phys. Rev. B **98**, 060411(R) (2018).

[27] A. O. Leonov, C. Pappas, and I. Kézsmárki, Field and anisotropy driven transformations of spin spirals in cubic skyrmion hosts, Phys. Rev. Research **2**, 043386 (2020).

[28] E. C. Gartland, H. Huang, O. D. Lavrentovich, P. Palffy-Muhoray, I. I. Smalyukh, T. Kosa, and B. Taheri, Electric-field induced transitions in a cholesteric liquid-crystal film with negative dielectric anisotropy, J. Comput. Theor. Nanosci. **7**, 709 (2010).

[29] G. De Matteis, L. Martina, C. Naya, and V. Turco, Helicoids in chiral liquid crystals under external fields, Phys. Rev. E **100**, 052703 (2019).

[30] S. Afghah and J. V. Selinger, Theory of helicoids and skyrmions in confined cholesteric liquid crystals, Phys. Rev. E **96**, 012708 (2017).

[31] A. Y. Val'kov, E. V. Aksenova, and V. P. Romanov, First-order and continuous fréedericksz transitions in cholesteric liquid crystals, Phys. Rev. E **87**, 022508 (2013).

[32] P. F. Bessarab, V. M. Uzdin, and H. Jónsson, Method for finding mechanism and activation energy of magnetic transitions, applied to skyrmion and antivortex annihilation, Comput. Phys. Commun. **196**, 335 (2015).

[33] I. S. Lobanov, M. N. Potkina, H. Jónsson, and V. M. Uzdin, Truncated minimum energy path method for finding first order saddle points, Nanosyst. Phys. Chem. Math. **8**, 586 (2017).

[34] G. P. Müller, P. F. Bessarab, S. M. Vlasov, F. Lux, N. S. Kiselev, S. Blügel, V. M. Uzdin, and H. Jónsson, Duplication, Collapse, and Escape of Magnetic Skyrmions Revealed Using a Systematic Saddle Point Search Method, Phys. Rev. Lett. **121**, 197202 (2018).

[35] P. F. Bessarab, V. M. Uzdin, and H. Jónsson, Harmonic transition-state theory of thermal spin transitions, Phys. Rev. B **85**, 184409 (2012).

[36] I. S. Lobanov, H. Jónsson, and V. M. Uzdin, Mechanism and activation energy of magnetic skyrmion annihilation obtained from minimum energy path calculations, Phys. Rev. B **94**, 174418 (2016).

[37] V. Uzdin, M. Potkina, I. Lobanov, P. Bessarab, and H. Jónsson, Energy surface and lifetime of magnetic skyrmions, J. Magn. Magn. Mater. **459**, 236 (2018), the selected papers of Seventh Moscow International Symposium on Magnetism (MISM-2017).

[38] P. Oswald, J. Baudry, and S. Pirkl, Static and dynamic properties of cholesteric fingers in electric field, Phys. Rep. **337**, 67 (2000).

[39] I. I. Smalyukh, B. I. Senyuk, P. Palffy-Muhoray, O. D. Lavrentovich, H. Huang, E. C. Gartland, V. H. Bodnar, T. Kosa, and B. Taheri, Electric-field-induced nematic-cholesteric transition and three-dimensional director structures in homeotropic cells, Phys. Rev. E **72**, 061707 (2005).

[40] See Supplemental Material at http://link.aps.org/supplemental/10.1103/PhysRevE.105.034701 for videos illustrating the behavior of the toron and the skyrmion tube.